GEOPHYSICS®

3D elastic full-waveform inversion of surface waves in the presence of irregular topography using an envelope-based misfit function

SCHOLARONE™
Manuscripts

Geophysics   1

3D ELASTIC FULL-WAVEFORM INVERSION OF SURFACE WAVES IN THE PRESENCE OF IRREGULAR TOPOGRAPHY USING AN ENVELOPE-BASED MISFIT FUNCTION

Dmitry Borisov* (dborisov@princeton.edu), Ryan Modrak* (rmodrak@gmail.com),

Fuchun Gao[‡] (fuchun.gao@total.com) and Jeroen Tromp*[†]□ (jtromp@princeton.edu)

*Princeton University, Department of Geosciences, Princeton, New Jersey, USA.

[†]Princeton University, Program in Applied & Computational Mathematics, Princeton,

New Jersey, USA.

□[‡]Total E&P Research and Technology, Houston, Texas, USA.

Running head: 3D elastic FWI using envelopes

Geophysics   2

ABSTRACT

Full-waveform inversion (FWI) is a powerful method for estimating the Earth's material properties. We demonstrate that surface-wave driven FWI is well-suited to recovering near-surface structures and effective at providing shear wavespeed starting models for use in conventional body-wave FWI. We illustrate the method with a synthetic example based on the SEAM Phase II foothills model. To accurately model surface waves in the presence of complex tomography, we used a spectral-element wave propagation solver. We started first with an envelope-based objective function to invert for shallow large-scale heterogeneities. Then using the recovered model of the subsurface, we applied a waveform-difference inversion to obtain higher-resolution models. Envelope misfit functions were found to be effective in minimizing cycle-skipping issues for surface-wave inversions, which are useful for constraining complex near-surface features.

INTRODUCTION

Elastic full-waveform inversion (FWI), introduced by Lailly (1983) and Tarantola (1984), is a data-fitting procedure for estimating elastic properties (i.e., compressional and/or shear wavespeeds). The technique has proven to be particularly efficient for retrieval of P-wave structure using transmitted energy (e.g., diving or refracted waves) (Shipp and Singh, 2002; Virieux and Operto, 2009). The technique consists of minimizing differences between observed and synthetic seismograms through an iterative local optimization process. The gradient of the data misfit for the model update at each iteration is efficiently calculated using an adjoint-state method (Chavent, 1974; Tromp et al., 2005; Plessix, 2006). Compared to first-arrival traveltime tomography, FWI models generally have better resolution, which often leads to an improved

migrated image (e.g., Sirgue et al., 2010). However, the technique frequently suffers from cycle-skipping artifacts between observed and predicted data. Thus, the updated model can become trapped in a local minimum due to an inaccurate starting model, limited source-receiver offset ranges, or lack of reliable low-frequency information.

In land surveys, seismic traces recorded at the surface are dominated by high-amplitude, dispersive surface waves. Surface waves decay exponentially with depth and most of their energy is confined within a depth of about half a wavelength from the free surface. While surface waves have been utilized in other disciplines, including ultrasonic acoustics, geotechnical engineering, nondestructive testing, archaeological studies, near-surface geophysics, and global seismology (e.g., Socco et al., 2010), in seismic exploration studies for imaging deeper structures, they are commonly treated as noise (conventionally referred to as ground-roll or guided waves). Mitigation of this noise is required for imaging smaller reflected signals, but can be challenging because surface waves propagate as multiple modes, each with its own dispersive characteristics.

In this study we work in the elastic formulation and explore the use of surface waves as an additional source of information on the shallow subsurface. Conventional methods for near-surface inversion include spectral analysis of surface waves (SASW) (Nazarian and Stokoe, 1984) and multichannel analysis of surface waves (MASW) (Park et al., 1999; Xia et al., 1999). Analyses of dispersion curves based on use of f-k or radon transforms for a multichannel array can facilitate construction of local one-dimensional profiles, but are inherently limited in the ability to handle lateral variations. FWI is a more general technique for dealing with surface waves as, in theory, it can utilize the complete wavefield recorded in seismographic networks to

build high-resolution three-dimensional (3D) models. However, inversion of surface waves requires special treatment, because it makes conventional waveform-difference (WD) objective functions highly sensitive to the initial model due to increasingly nonlinear behavior of the misfit function (Brossier et al., 2009). Recently, several surface-wave FWI studies waves using alternative misfit functions have been published (e.g., Masoni et al., 2013; Solano et al., 2014). Here, we extend the approach of Yuan et al. (2015) to three dimensions, using an envelope-difference (ED) misfit function for inverting surface-wave dominated records in the early stages of the inversion to improve shallow constraints on P and S wavespeeds. Reliable 3D model of the near surface could improve reconstruction of deeper structure in later stages, when inverting body waves using WD misfit function.

We consider strong topographic variations in our inversion example. Irregular topography is known to have a significant impact on seismic wave propagation. For instance, it can distort wavefronts by scattering and reflecting waves in a complex fashion. It also amplifies the wavefield at mountain tops and reduces ground motion in lowlands (e.g., Geli et al., 1988). For FWI, it was reported that neglecting topography with amplitude variations greater than half the minimum wavelength leads to significant inversion artifacts (Nuber et al., 2016). It is expected that two-dimensional (2D) assumptions cannot fully approximate wave propagation in the presence of substantial 3D topography. Therefore, the ground surface should be accurately represented in waveform inversion. To handle strong variations in topography, we use a solver based on the spectral-element method (SEM) (Komatitsch and Vilotte, 1998; Komatitsch and Tromp, 1999). This method is particularly well suited for accurate wavefield simulations in complex geological settings.

This paper is organized as follows. Section 2 describes the forward modeling and waveform inversion algorithm adopted in our study. Section 3 provides a synthetic example justifying our inversion approach. We perform 3D elastic FWI on the data simulated using the 3D SEAM Phase II foothills model (from hereon referred to as the SEAM model) (Oristaglio, 2012), which is based on a complex realistic onshore model. Finally, in section 4, we summarize our work and discuss future directions.

METHOD AND ALGORITHM

The FWI algorithm can be divided in two major parts, summarized briefly in the following subsections: the forward problem and the inverse problem.

Forward problem

In our study we use the spectral-element solver SPECFEM3D (Peter et al., 2011), which is capable of simulating forward and adjoint wavefields on hexahedral conforming meshes. Unlike in classical finite-element schemes, use of Lagrange interpolants in combination with Gauss-Lobatto-Legendre (GLL) quadrature renders the mass matrix diagonal. Time discretization is based on a Newmark scheme, which is an explicit second-order finite-difference (FD) scheme (Hughes, 2012). Our particular implementation includes both MPI parallelization and GPU acceleration (Komatitsch et al., 2009). To absorb undesirable outgoing waves from the model boundaries we use Clayton-Engquist-Stacey absorbing conditions (Clayton and Engquist, 1977; Stacey, 1988). Perfectly Matched Layer (PML) (Berenger, 1994) boundary conditions, or its improved version with an unsplit convolutional formulation (CPML), (Komatitsch and Martin, 2007) are currently being implemented and will provide better accuracy in future work.

Finally, because of the weak formulation of the spectral-element method, the free surface

boundary condition is explicitly taken into account, thereby providing stable, accurate

simulations even in regions with complex topography (Komatitsch and Vilotte, 1998;

Komatitsch and Tromp, 1999).

To demonstrate the importance of incorporating topography, we simulate seismic wave

propagation in the SEAM model (Figure 1). The approximate dimensions of the model are 14.5

km × 12.5 km × 10 km in the x-, y- and z- directions, respectively. The model has strong lateral

variations and shallow heterogeneity. The rugged topography is taken from a region of the

Llanos foothills of Colombia with overall elevation differences of up to 1.6 km (Figure 2). The

quality of forward modeling in such challenging conditions with commonly used FD methods

will be strongly compromised because of staircase artifacts and inaccuracies related to the

implementation of the free-surface condition. It is worse mentioning that there are FD methods

formulated in curvilinear grids, which allow to alleviate this problem (Komatitsch et al., 1996).

The black dashed line in Figure 2 indicates the part of the full model selected for the

waveform inversion example described in the next section. The full mesh was built using an

internal SPECFEM3D mesher, which is efficient for models of low-to-moderate complexity. In

this case, the spatial distribution of geologic interfaces including topography and number of

spectral elements between interfaces should be specified before simulation. To mesh more

complex models, software such as CUBIT, TRELIS, or Gmsh may be used (Geuzaine and

Remacle, 2009) with the SPECFEM3D solver. To reduce skewness of the mesh due to abrupt

changes in the ground surface (i.e., Figure 3a), we used a smoothed topographic map (Figure 3b,

interface S2) beneath the model surface in the manner of Lee et al. (2009). The elevation in the

Geophysics   7

smoothed interface is about twice smaller than in the ground surface. We also used the same

smoothed topographic map as an interface below which the size of the elements is doubled. This

allows us to capture topographic variations very accurately with a fine mesh near the surface

while reducing the computational cost by using larger elements at depth. Moreover, typically

there is a wavespeed gradient, which allows use of larger elements in deeper parts of the model.

The average vertical dimension of elements above and beneath the doubling interface is 25 m

and 50 m, respectively.

For the source-time function we used a Ricker wavelet with a 15 Hz dominant frequency.

The effects of irregular topography are illustrated in Figure 4, where wavefield snapshots of the

norm of the particle velocity at the surface are shown for the model with topography (Figure 4a)

and without topography (Figure 4b) at 2.4 s. To produce the model with a flat topography, we cut

the portion above the lowest point in the actual model. Data records from the simulation are

shown in Figure 5. Because attenuation is not included in the simulation, most of the seismic

energy is propagated in the form of surface waves. From both the wavefield snapshots and record

sections it is clear that irregular topography scatters and reflects seismic waves in a very

pronounced way, and thus topography should be accurately accounted for in the inversion.

Inverse problem

In full-waveform inversion, we seek to minimize the difference between observed data

and corresponding synthetics. The goodness-of-fit is commonly measured as a least-squares (l_2)

waveform-difference misfit function (e.g., Tarantola, 1984; Mora, 1987). The gradient is formed

as a sum of all kernels, where each kernel is obtained from the crosscorrelation of forward and

adjoint wavefields. In our examples we use the L-BFGS quasi-Newton method for computing

search directions (Nocedal, 1980; Liu and Nocedal, 1989). We perform a safeguarded

backtracking line search (Modrak and Tromp, 2016) to calculate a step length.

As an alternative to the conventional least-squares WD misfit function, here we use the

ED misfit function in the manner of Yuan et al. (2015). Envelopes have been shown to yield

good measures of misfit in seismic inverse problems as they minimize cycle-skipping issues

(e.g., Bozdag et al., 2011; Wu et al., 2014). However, Wu et al. (2014) and Bharadwaj et al.

(2016) discussed some challenges related to combining FWI and envelope misfits. For instance,

the approach is not sensitive to traveltime errors that surpass the width of the predicted and

observed envelopes. In addition, the envelope-based misfit cannot retrieve long wavelength

heterogeneity using only reflected data. However, as shown by Yuan et al. (2015), the envelope

misfit function provides a robust measure for highly nonlinear surface-wave inversions. In the

next section, we show a 3D application complicated by the presence of irregular topography.

NUMERICAL EXAMPLE

We demonstrate our approach using the SEAM model (Figure 1). To reduce the overall

duration of the inversion, we select only a portion of the original model. The reduced volume is 7

km × 3.5 km × 3.3 km in the *x*-, *y*- and *z*-directions, respectively (Figure 6a). The model exhibits

strong variations in elevation, with differences up to 0.9 km. The mesh (Figure 6b) is constructed

before the inversion and there is no need to rebuild it in subsequent iterations. The total number

of mesh elements is 207,360. The total number of GLL points with duplicates on MPI edges is

about 14×10^6. There are two levels of parallelization, including one over sources and one for

domain decomposition. The total recording time is 5 s with a 1 ms time step. The simulation time

for a single source simulation is about 3 min using 96 MPI processors.

Geophysics   9

The true model contains strong lateral variations in material properties, with P and S wavespeeds (V_P and V_S, respectively) varying from 2.3 to 4.8 km/s and 1.2 to 2.5 km/s, respectively, and density varying from 2.09 to 2.6 kg/m^3. The shear wavespeed contrast in some locations is more than 1 km/s. It is worth mentioning that, for the acoustic approximation, the presence of strong contrasts in shear wavespeed and density produces unpredictable elastic effects in the observed data, which can significantly distort waveform inversion results (e.g., Solano et al., 2013; Borisov et al., 2014; Borisov and Singh, 2015). The V_P/V_S ratio varies from 1.76 to 2.06. Starting P and S wavespeeds and densities were obtained by applying a discretized spline smoothing to the target model.

For the inversion we used 72 sources and 2,502 receivers regularly distributed along the surface (Figure 7). The distance between shots is 600 m in the x- and y-directions, while the distance between receivers is 50 m and 200 m, respectively. Each source represents a force applied in the vertical direction with a Ricker wavelet source time function. We used a known source signature and the same spectral-element solver to generate observed and synthetic data, thus committed the inverse crime. In real data applications, the source time function is unknown but can be extracted from the data or estimated by solving a linear inverse problem (Pratt, 1999). Attenuation was not included in this example, but strong attenuation might severely complicate inversion convergence in case of real data. To alleviate the anelastic effects in surface-wave inversion, Baumstein et al. (2011) did not include Q, but found it important to apply a Q filter to the modeled data and to use a normalized crosscorrelation objective function. To make the inversion more difficult, we used relatively high frequencies (with a dominant frequency of 6 Hz) and did not employ a multiscale approach in the manner of Bunks et al. (1995), Yuan and Simons (2014), or Yuan et al. (2015). The corresponding wavelengths at the dominant frequency

Geophysics 10

range from 0.4 - 0.8 km for P-waves and 0.2 - 0.4 km for S-waves. A vertical force applied at the surface generates Rayleigh waves which are recorded by geophones. Only the vertical component of particle displacement is used for inversion. This choice was made because near-surface seismic surveys are often restricted to recording the vertical component.

Figure 8 shows a comparison between the true, initial, and inverted models. In this case we simultaneously inverted for P and S wavespeeds, while the density was kept constant. Although surface waves have minor sensitivity to density (Nazarian and Stokoe, 1984), inverting for density might provide better final models for both V_P and V_S (Yuan et al., 2015). Another option might be to update the density at each iteration using some empirical relationship involving P or S wavespeed (Sears et al., 2010). At the initial stage we used the ED misfit function while inverting the entire content of the seismograms. After 30 iterations the S wavespeed model is significantly improved in the shallow part (Figures 8e and 8f). We used this result as input for the WD-FWI. After another 30 iterations the results show further improvement (Figures 8g and 8h). Although the overall velocity structure is significantly improved, some small-scale features are still missing, e.g. a low-velocity stripe around $x = 1.2$ km on Figure 8h. The reason that some small-scale features do not appear in the inversion results might be related to the frequency content or insufficient number of inversion iterations. The misfit curve on Figure 9 confirms that additional iterations using envelope FWI can further improve the results, as the convergence was not reached. Figure 10 shows the recovery of the V_P model. Compared to the V_S results, the V_P model is not as good. First of all, the data is dominated by surfaces waves, which are much more sensitive to V_S information. Moreover, the V_S model is better resolved due to a shorter wavelength, i.e. smaller features can be retrieved in the V_S model for the same frequency content in the data.

Geophysics   11

Figure 11 shows vertical profiles for V_S (panels a, b and c) and for V_P (panels d, e and f)

in the target, initial, ED-FWI and final models at three different locations. Profiles (a) and (d) are

located at $x = 1.5$ km and $y = 1.75$ km. Profiles (b) and (e) are located at $x = 3.5$ km and $y = 1.75$

km. Profiles (c) and (f) are located at $x = 5.5$ km and $y = 1.75$ km. It can be observed that most

updates are confined to the region within the first kilometer from the surface, where the V_S

results are significantly improved. Once again, there are very small updates in the V_P results. To

analyze the resolution of the inversion as a function of depth from the surface we calculated the

volume of investigation (VOI) (Oldenburg and Li, 1999; Oldenborger et al., 2007). The VOI is

calculated according to the difference equation:

$$voi = \frac{m_2 - m_1}{m_2^{init} - m_1^{init}}, \tag{1}$$

where m_2 is the model obtained via inversion with initial model m_2^{init} and m_1 is the model

obtained via inversion with reference model m_1^{init}. The initial model m_1^{init} is used in the first

synthetic experiment, whereas m_2^{init} is the initial model increased by 5% and used in the second

inversion experiment described at the end of this section. The VOI approaches zero in the

regions where the model is reliable, otherwise it approaches unity, and actually can be

unbounded in case of highly non-unique problems. The computed VOI values suggest that most

of reliable updates are coming from the region within 1.5 km and 0.3 km from the surface for V_S

and V_P, respectively.

Trace by trace normalized source records and corresponding envelopes for the shot

located at $x = 1.0$ km, $y = 1.75$ km are shown in Figure 13. As the shallow part of the true model

contains strong heterogeneities, observed data are dominated by strong amplitude and dispersive

Rayleigh waves. In contrast, surface waves in the initial synthetics are much less dispersive

because the starting model is relatively smooth. It is clear that the synthetic shot gather generated

from a model inverted using envelope-based FWI agrees much more closely with the observed

one. Figure 14 shows residual shot records and difference between observed and synthetic

envelopes before and after inversion. In general, the amplitude of the residuals is decreased over

all offsets. Additional ED and WD iterations might be required to further reduce residuals, as

there are a few remaining packages of energy, particularly in waveforms residuals at near and far

offsets (Figure 14c). If we zoom in on an initial comparison of a few traces, we find that at far

offsets (traces plotted in the lower part of the panel) the surface waves are cycle-skipped,

whereas the difference between the corresponding envelopes is not as pronounced (Figure 15).

Moreover, comparison of amplitude spectra for a single trace at far offset shows the emergence

of ultra-low frequencies in the envelope (Figure 16), which promotes convergence to the global

minimum.

It is worth mentioning that WD-FWI applied directly to the same observed data without

ED-FWI, failed after a few unsuccessful trials of finding an adequate step length that reduced the

misfit function. Normalized gradients from the first iteration are compared in Figure 17. The ED-

FWI gradient in the shallow part on the right side (red dashed box) is positive, which enables the

wavespeed reduction in that region. This indicates that the inversion produces S wavespeed

updates in the right direction (Figure 8a). However, the WD-FWI gradient in the same area is

negative, which pushes the wavespeed update in the wrong direction.

We also performed an experiment with less accurate starting model. We used starting

models increased by 5% of their true values instead of using simply smoothed versions of the

target models. The inversion results for V_S and V_P wavespeeds are shown on Figures 18 and 19,

respectively. It took twice more iterations at the first stage of inversion to converge. Although the results are little bit less accurate, similar observations can be made as in the first inversion example. While the overall V_S structure is significantly improved, the are very small updates in the V_P results.

CONCLUSION

We perform 3D elastic FWI of surface and body waves in the presence of strong wavespeed contrasts and topographic variations. An envelope-based misfit function is shown to be effective for inverting seismograms dominated by surface waves. A synthetic example for the 3D SEAM Phase II foothills model illustrates that inversion of surface waves at the initial stages furnishes an improved starting shear wavespeed model for traditional FWI.

Irregular topography has a significant impact on seismic wave propagation. It distorts seismic wavefronts by scattering and reflecting seismic waves in a complex way. The elevation difference in our example is between 2 and 4 shear wavelengths. Accurate wavefield modeling using a 3D elastic spectral-element method is an important ingredient for successful waveform inversions in such challenging geological settings. In our study we have assumed a constant density. In reality, one might consider inverting for density as well, but the sensitivity of surface waves to this parameter is rather poor. Moreover, density is known to be difficult to invert. As is typical for near-surface seismic inversion, only the vertical component of the data was used. We have found that an inversion restricted to the data recorded on vertical axis can provide adequate results. However, this kind of data decimation may result in a reduced resolution. Our surface-wave inversion method is effective at improving recovery of near-surface structure. Future work

Geophysics 14

will focus on applications to field data, with several challenging field acquisitions already
underway.

ACKNOWLEDGMENTS

Geophysics   15

REFERENCES

Baumstein, A., W. Ross, and S. Lee, 2011, Simultaneous source elastic inversion of surface waves: Presented at the 73rd EAGE Conference and Exhibition incorporating SPE EUROPEC 2011.

Berenger, J.-P., 1994, A perfectly matched layer for the absorption of electromagnetic waves: Journal of Computational Physics, 114, 185–200.

Bharadwaj, P., W. Mulder, and G. Drijkoningen, 2016, Full waveform inversion with an auxiliary bump functional: Geophysical Journal International, 206, 1076–1092.

Borisov, D., and S. C. Singh, 2015, Three-dimensional elastic full waveform inversion in a marine environment using multicomponent ocean-bottom cables: a synthetic study: Geophysical Journal International, 201, 1215–1234.

Borisov, D., A. Stopin, and R. Plessix, 2014, Acoustic pseudo-density full waveform inversion in the presence of hard thin beds: Presented at the 76th EAGE Conference and Exhibition 2014.

Bozdağ, E., J. Trampert, and J. Tromp, 2011, Misfit functions for full waveform inversion based on instantaneous phase and envelope measurements: Geophysical Journal International, 185, 845–870.

Brossier, R., S. Operto, and J. Virieux, 2009, Seismic imaging of complex onshore structures by 2D elastic frequency-domain full-waveform inversion: Geophysics, 74, no.6, WCC105– WCC118.

Geophysics 16

Bunks, C., F. M. Saleck, S. Zaleski, and G. Chavent, 1995, Multiscale seismic waveform inversion: Geophysics, 60, 1457–1473.

Chavent, G., 1974, Identification of functional parameters in partial differential equations: Joint Automatic Control Conference, 155–156.

Clayton, R., and B. Engquist, 1977, Absorbing boundary conditions for acoustic and elastic wave equations: Bulletin of the Seismological Society of America, 67, 1529–1540.

Geli, L., P.-Y. Bard, and B. Jullien, 1988, The effect of topography on earthquake ground motion: a review and new results: Bulletin of the Seismological Society of America, 78, 42–63.

Geuzaine, C., and J.-F. Remacle, 2009, Gmsh: A 3-D finite element mesh generator with built-in pre-and post-processing facilities: International Journal for Numerical Methods in Engineering, 79, 1309–1331.

Hughes, T. J., 2012, The finite element method: linear static and dynamic finite element analysis: Courier Corporation.

Komatitsch, D., F. Coutel, and P. Mora, 1996, Tensorial formulation of the wave equation for modelling curved interfaces: Geophysical Journal International, 127, 156–168.

Komatitsch, D., and R. Martin, 2007, An unsplit convolutional perfectly matched layer improved at grazing incidence for the seismic wave equation: Geophysics, 72, no.5, SM155–SM167.

Geophysics 17

Komatitsch, D., D. Michéa, and G. Erlebacher, 2009, Porting a high-order finite-element earthquake modeling application to NVIDIA graphics cards using CUDA: Journal of Parallel and Distributed Computing, 69, 451–460.

Komatitsch, D., and J. Tromp, 1999, Introduction to the spectral element method for three- dimensional seismic wave propagation: Geophysical Journal International, 139, 806–822.

Komatitsch, D., and J.-P. Vilotte, 1998, The spectral element method: An efficient tool to simulate the seismic response of 2D and 3D geological structures: Bulletin of the Seismological Society of America, 88, 368–392.

☐Lailly, P., 1983, The seismic inverse problem as a sequence of before stack migrations: Conference on inverse scattering: theory and application, Society for Industrial and Applied Mathematics, Philadelphia, PA, 206–220.☐

Lee, S.-J., D. Komatitsch, B.-S. Huang, and J. Tromp, 2009, Effects of topography on seismic-wave propagation: An example from northern Taiwan: Bulletin of the Seismological Society of America, 99, 314–325.☐

Liu, D. C., and J. Nocedal, 1989, On the limited memory BFGS method for large scale optimization: Mathematical programming, 45, 503–528.☐

Masoni, I., R. Brossier, J. Virieux, and J. Boelle, 2013, Alternative misfit functions for FWI applied to surface waves: Presented at the 75th EAGE Conference & Exhibition incorporating SPE EUROPEC 2013.☐

Geophysics   18

Modrak, R., and J. Tromp, 2016, Seismic waveform inversion best practices: regional, global and exploration test cases: Geophysical Journal International, 206, 1864–1889.□

Mora, P., 1987, Nonlinear two-dimensional elastic inversion of multioffset seismic data: Geophysics, 52, 1211–1228.□

Nazarian, S., and K. Stokoe, 1984, In situ shear wave velocities from spectral analysis of surface waves: 8th Conference on Earthquake Engineering, vol. 3, 31–38.

□Nocedal, J., 1980, Updating quasi-Newton matrices with limited storage: Mathematics of Computation, 35, 773–782.□

Nuber, A., E. Manukyan, and H. Maurer, 2016, Ground topography effects on near-surface elastic full waveform inversion: Geophysical Journal International, 207, 67–71.

Oldenborger, G. A., P. S. Routh, and M. D. Knoll, 2007, Model reliability for 3D electrical resistivity tomography: Application of the volume of investigation index to a time-lapse monitoring experiment: Geophysics, 72, no.4, F167–F175.□

Oldenburg, D. W., and Y. Li, 1999, Estimating depth of investigation in DC resistivity and IP surveys: Geophysics, 64, 403–416.

□Oristaglio, M., 2012, SEAM Update: SEAM Phase II-surface waves in land seismic exploration: The Leading Edge, 31, 1130–1132.□

Park, C. B., R. D. Miller, and J. Xia, 1999, Multichannel analysis of surface waves: Geophysics, 64, 800–808.□

Geophysics   19

Peter, D., D. Komatitsch, Y. Luo, R. Martin, N. Le Goff, E. Casarotti, P. Le Loher, F. Magnoni, Q. Liu, C. Blitz, et al., 2011, Forward and adjoint simulations of seismic wave propagation on fully unstructured hexahedral meshes: Geophysical Journal International, 186, 721–739.

Plessix, R.-E., 2006, A review of the adjoint-state method for computing the gradient of a functional with geophysical applications: Geophysical Journal International, 167, 495– 503.

Pratt, R. G., 1999, Seismic waveform inversion in the frequency domain, Part 1: Theory and verification in a physical scale model: Geophysics, 64, 888–901.

Sears, T. J., P. J. Barton, and S. C. Singh, 2010, Elastic full waveform inversion of multi-component ocean-bottom cable seismic data: Application to Alba Field, UK North Sea: Geophysics, 75, no.6, R109–R119.

Shipp, R. M., and S. C. Singh, 2002, Two-dimensional full wavefield inversion of wide-aperture marine seismic streamer data: Geophysical Journal International, 151, 325–344.

Sirgue, L., O. Barkved, J. Dellinger, J. Etgen, U. Albertin, and J. Kommedal, 2010, The-matic set: Full waveform inversion: The next leap forward in imaging at Valhall: First Break, 28, 65–70.□

Socco, L. V., S. Foti, and D. Boiero, 2010, Surface-wave analysis for building near-surface velocity models - Established approaches and new perspectives: Geophysics, 75, no.5, 75A83–75A102.

Geophysics   20

Solano, C. P., D. Donno, and H. Chauris, 2014, Alternative waveform inversion for surface wave analysis in 2-D media: Geophysical Journal International, 198, 1359–1372.

Solano, C. P., A. Stopin, and R. Plessix, 2013, Synthetic study of elastic effects on acoustic full waveform inversion: Presented at the 75th EAGE Conference & Exhibition incorporating SPE EUROPEC 2013.

Stacey, R., 1988, Improved transparent boundary formulations for the elastic-wave equation: Bulletin of the Seismological Society of America, 78, 2089–2097.

Tarantola, A., 1984, Inversion of seismic reflection data in the acoustic approximation: Geophysics, 49, 1259–1266.

Tromp, J., C. Tape, and Q. Liu, 2005, Seismic tomography, adjoint methods, time reversal and banana-doughnut kernels: Geophysical Journal International, 160, 195–216.

Virieux, J., and S. Operto, 2009, An overview of full-waveform inversion in exploration geophysics: Geophysics, 74, no.6, WCC1–WCC26.

Wu, R.-S., J. Luo, and B. Wu, 2014, Seismic envelope inversion and modulation signal model: Geophysics, 79, no.3, WA13–WA24.

Xia, J., R. D. Miller, and C. B. Park, 1999, Estimation of near-surface shear-wave velocity by inversion of Rayleigh waves: Geophysics, 64, 691–700.

Yuan, Y. O., and F. J. Simons, 2014, Multiscale adjoint waveform-difference tomography using wavelets: Geophysics, 79, no.3, WA79–WA95.

Geophysics

21

Yuan, Y. O., F. J. Simons, and E. Bozdaǧ, 2015, Multiscale adjoint waveform

tomography for surface and body waves: Geophysics, 80, no.5, R281–R302.

LIST OF FIGURES

Geophysics   23

7 Acquisition layout for the FWI experiment. Red and black dots indicate sources and receivers, respectively.

8 S wavespeed results from the first inversion example. Vertical slices at $y = 1.75$ km (left) and horizontal slices at 1.7 km depth (right). True (a, b), initial (c, d), envelope-difference FWI (e, f), and waveform-difference FWI (g, h) models. Note how the S wavespeed model is significantly improved in the shallow part after applying two stages of FWI.

9 Normalized misfit values from the first inversion experiment. 30 iterations of envelope FWI were followed by 30 iterations of waveform-difference FWI. The overall misfit is reduced by more than 90%, but additional iterations using envelope FWI can possibly further improve the results, as the convergence was not reached.

10 P wavespeed results from the first inversion example. Vertical slices at $y = 1.75$ km (left) and horizontal slices at 1.7 km depth (right). True (a, b), initial (c, d), envelope-difference FWI (e, f), and waveform-difference FWI (g, h) models. Note that compared to the V_S results (Figure 8), the V_P model is not as good.

11 Vetrical profiles in the target, initial, ED-FWI and final models for S (a, b and c) and P (d, e and f) wavespeeds from the first inversion example. Profiles (a) and (d) are located at $x = $ 1.5 km and $y = 1.75$ km. Profiles (b) and (e) are located at x=3.5 km and y=1.75 km. Profiles (c) and (f) are located at $x = 5.5$ km and $y = 1.75$ km. Most updates are confined to the region within the first kilometer from the surface, where the V_S results are significantly improved. There are very small updates in the V_P results.

Geophysics

24

12 Volume of investigation (VOI) function calculated for S (top) and P (bottom) wavespeeds, respectively. The computed VOI values suggest that most of reliable updates are coming from the region within 1.5 km and 0.3 km from the surface for V_S and V_P, respectively.

13 Trace by trace normalized shot records of vertical component of particle displacement (left) and corresponding envelopes (right) from the FWI example. Observed records (a, b), initial synthetics (c, d) and synthetics after envelope FWI (e, f). Observed data are dominated by strong amplitude and dispersive Rayleigh waves. The final synthetics agree much more closely with the observed data.

14 Initial and final data residuals (a, c); difference between observed and synthetic envelopes before (b) and after (d) inversion, respectively. In general, the amplitude of the residuals is decreased over all offsets. Additional inversion iterations might be required to further reduce residuals at near and far offsets.

15 Initial (left) and final (right) comparison of trace by trace normalized records of vertical component of particle displacement. Waveform (a, b) and corresponding envelope (c, d) traces. Traces are located between 2 km and 6.2 km, spaced by 0.6 km in the x-direction. At far offsets (lower part of each panel) the surface waves are cycle-skipped, whereas the difference between the corresponding envelopes is not as pronounced.

16 Amplitude spectrum for one trace and for its envelope. The receiver is located at $x = 6.0$ km. Note the presence of near-zero frequencies in the envelope spectrum which promotes convergence to the global minimum.

Geophysics   25

17 First iteration gradients of S wavespeed for envelope-difference based FWI (a) and for waveform-difference based FWI (b). The ED-FWI gradient in the shallow part on the right side (red dashed box) is positive, which enables the wavespeed reduction in that region. The WD-FWI gradient in the same area is negative, which pushes the wavespeed update in the wrong direction.

18 S wavespeed results from the second inversion experiment with a starting model increased by 5%. Vertical slices at $y = 1.75$ km (left) and horizontal slices at 1.7 km depth (right). Initial (a, b), envelope-difference FWI (c, d), and waveform-difference FWI (e, f) models. The overall V_S structure in the shallow part is significantly improved. □

19 P wavespeed results from the second inversion experiment with a starting model increased by 5%. Vertical slices at $y = 1.75$ km (left) and horizontal slices at 1.7 km depth (right). Initial (a, b), envelope-difference FWI (c, d), and waveform-difference FWI (e, f) models. Note that compared to the V_S results (Figure 18), the V_P model is not as good.
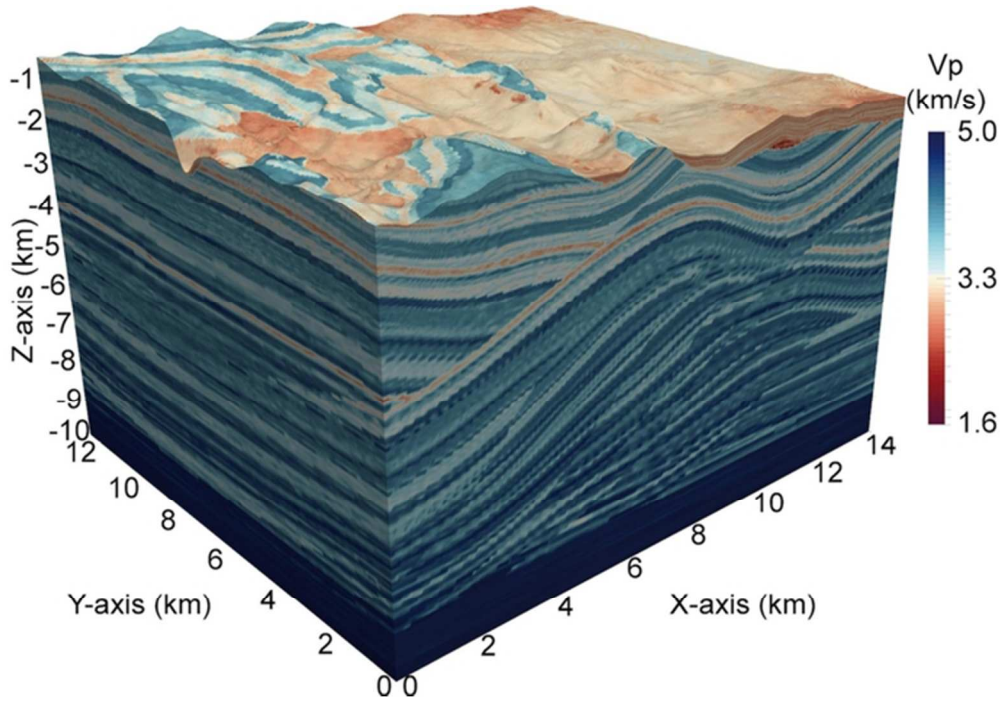
1. SEAM Phase II foothills model, three-dimensional P wavespeed variations. Note the significant topographic fluctuations and strong lateral variations.

58x40mm (300 x 300 DPI)
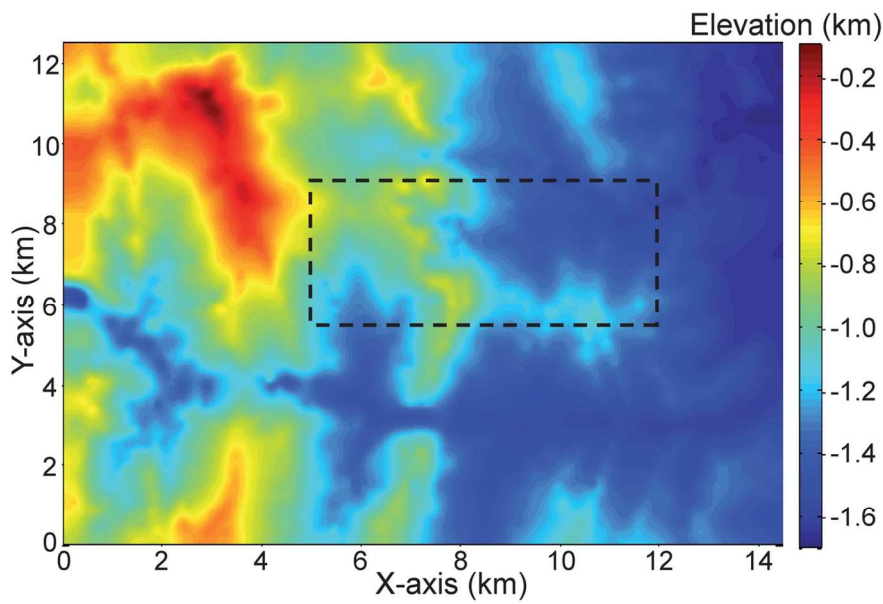
2. Elevation differences in the SEAM Phase II foothills model. The black dashed box indicates the part of the full model selected for the waveform inversion example described in section 3.

129x79mm (300 x 300 DPI)
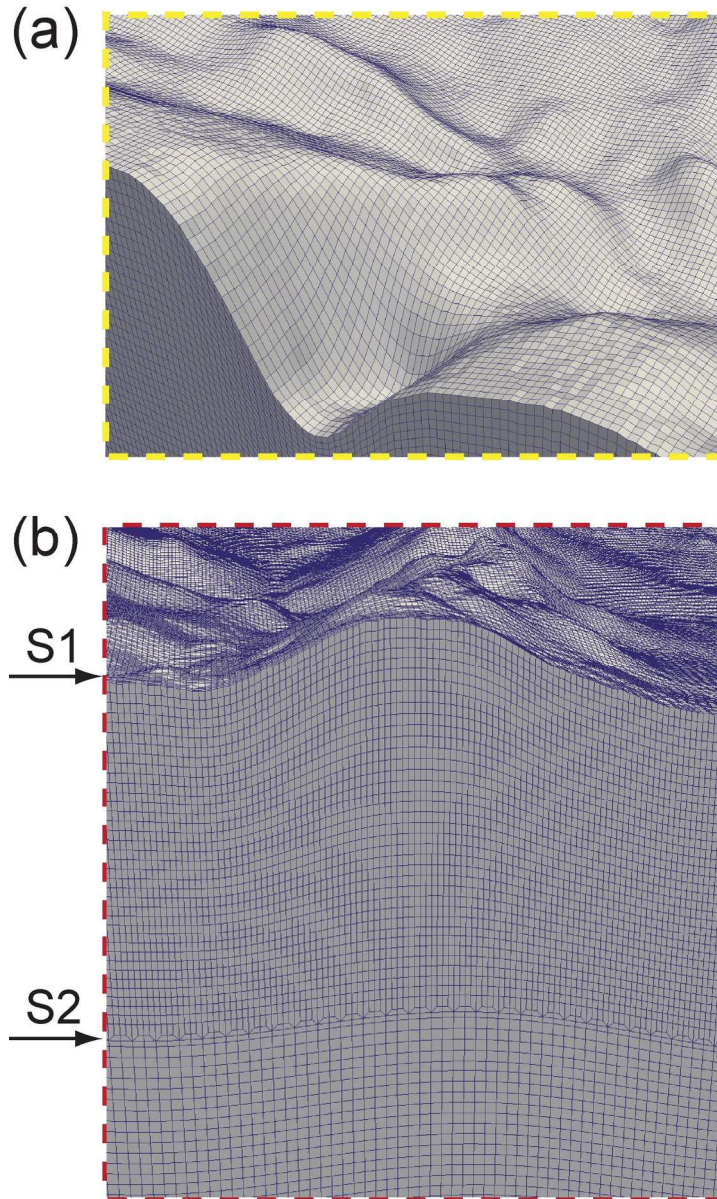
3. Close-up of two mesh regions. (a) One challenging region with steep slopes located around x = 0 km and y = 6 km. (b) Zoom on the inline section going through y = 0 km. S1 indicates surface topography; interface S2 represents a smoothed topographic map to prevent mesh distortions. The size of the elements is doubled below interface S2.

136x227mm (300 x 300 DPI)
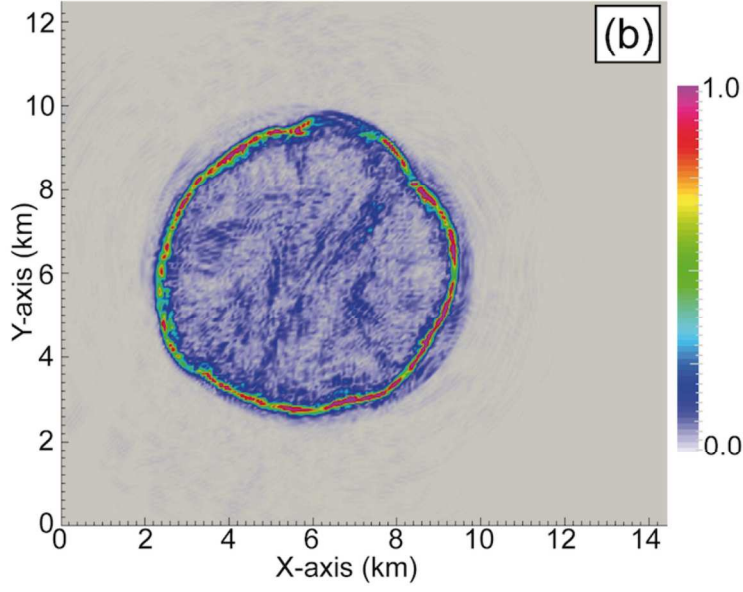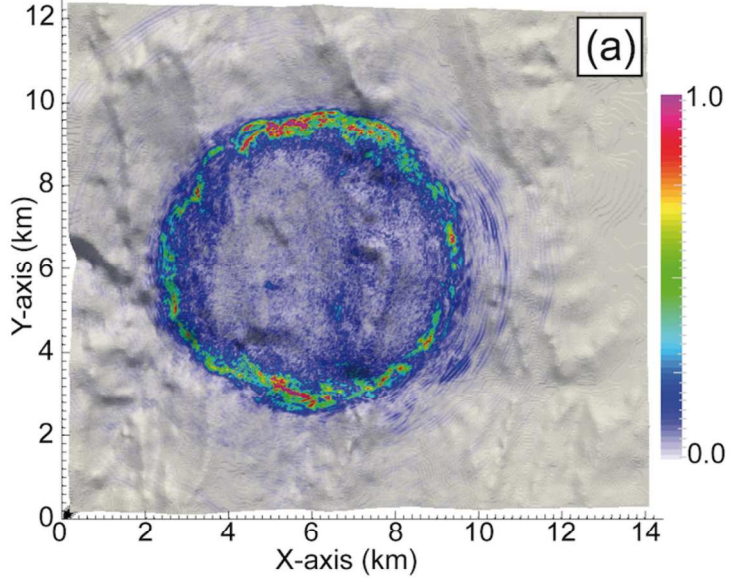
4. Snapshots of the norm of the particle velocity wavefield recorded at the surface at time 2.34 s from the simulation on the SEAM Foothills phase II model with actual topography (a) and with flat topography (b). Irregular topography scatters and reflects seismic waves in a very pronounced way.

137x223mm (300 x 300 DPI)
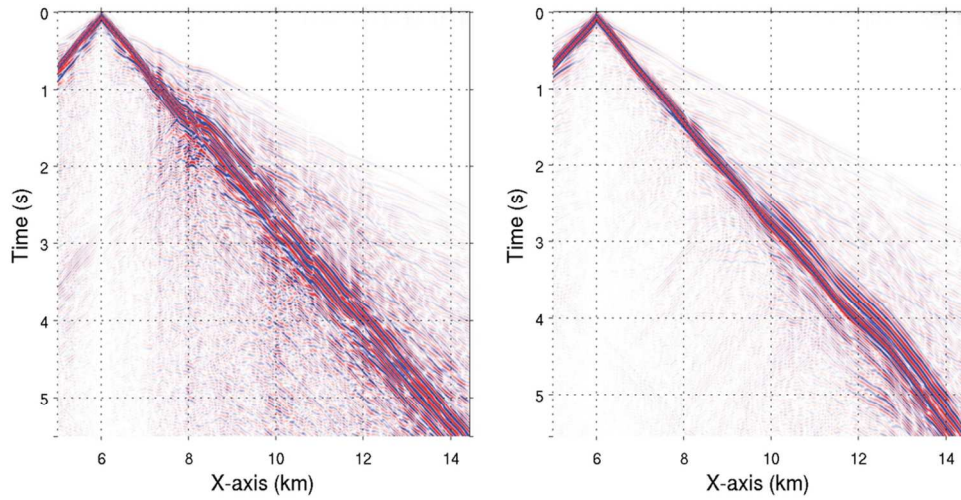
5. Shot gather of vertical component of particle displacement generated from a vertical source at (6,6) km in (x, y) and recorded along x-axis from the simulation on the SEAM Phase II foothills model with actual topography (left) and with a flat surface (right).

101x51mm (300 x 300 DPI)
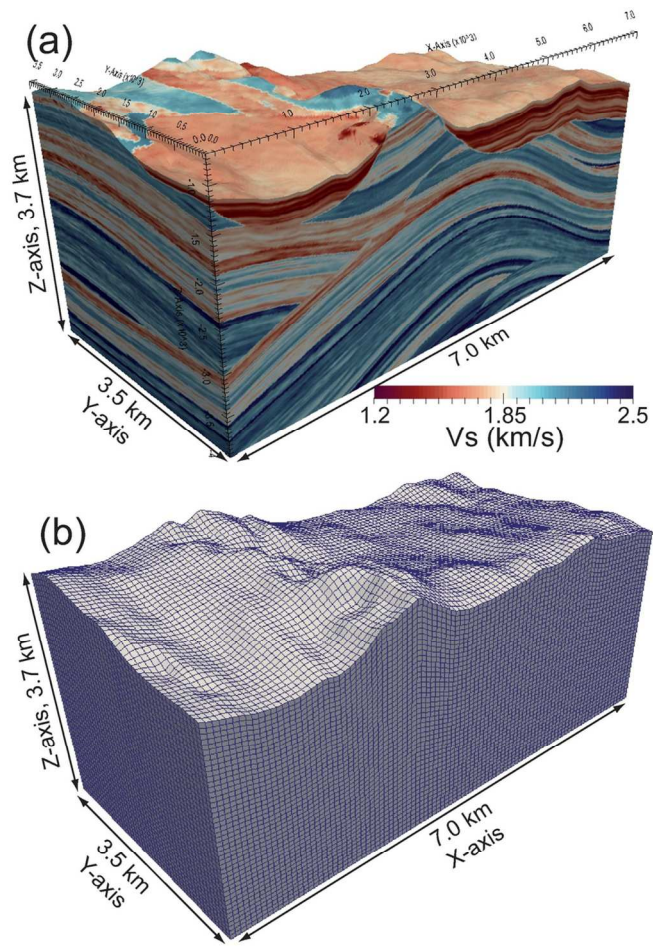
6. Portion of the 3D SEAM Phase II foothills model used for the FWI example. Shear wavespeed model (a) and corresponding mesh (b).

119x113mm (300 x 300 DPI)
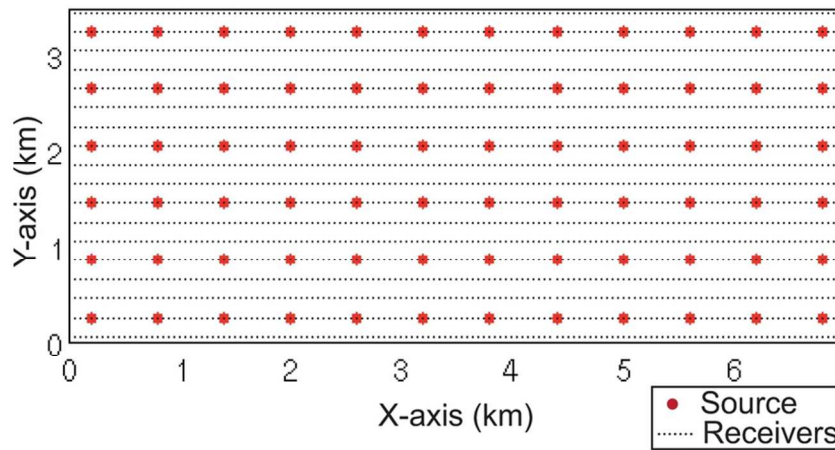
7. Acquisition layout for the FWI experiment. Red and black dots indicate sources and receivers, respectively.

89x43mm (300 x 300 DPI)
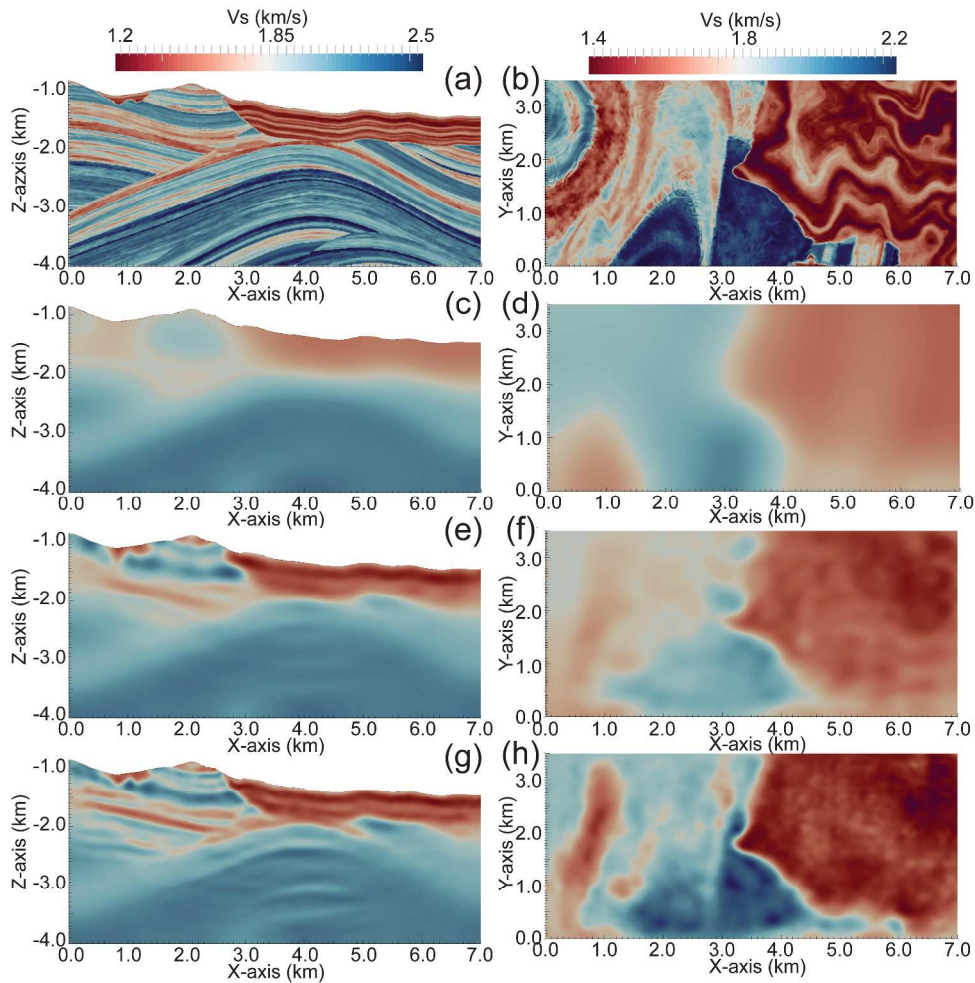
8. S wavespeed results from the first inversion example. Vertical slices at y = 1.75 km (left) and horizontal slices at 1.7 km depth (right). True (a, b), initial (c, d), envelope-difference FWI (e, f), and waveform-difference FWI (g, h) models. Note how the S wavespeed model is significantly improved in the shallow part after applying two stages of FWI.

431x421mm (300 x 300 DPI)
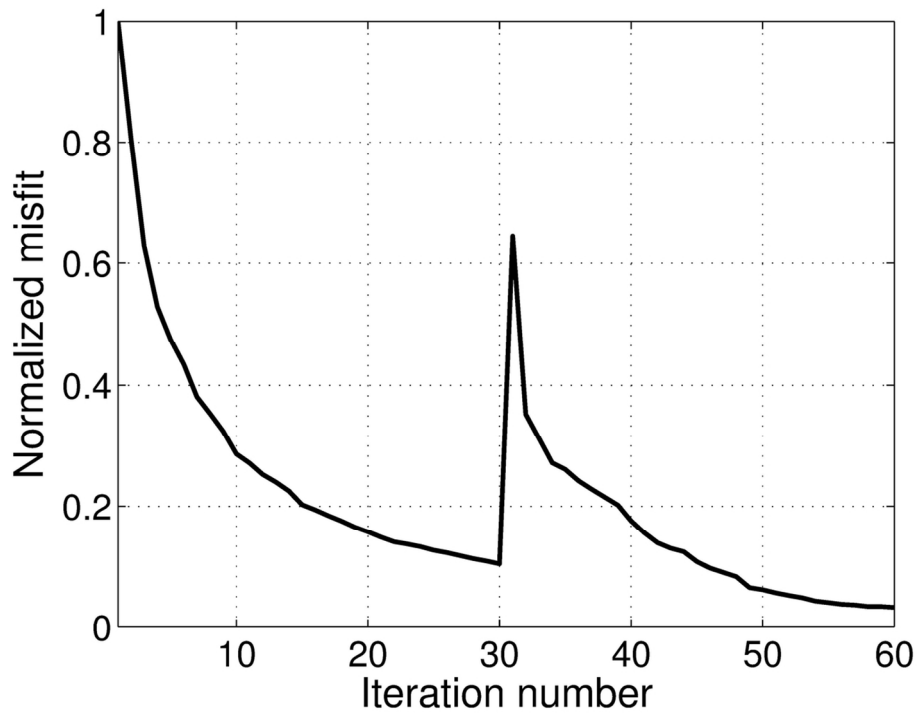
9. Normalized misfit values from the first inversion experiment. 30 iterations of envelope FWI were followed by 30 iterations of waveform-difference FWI. The overall misfit is reduced by more than 90%, but additional iterations using envelope FWI can possibly further improve the results, as the convergence was not reached.

118x89mm (300 x 300 DPI)
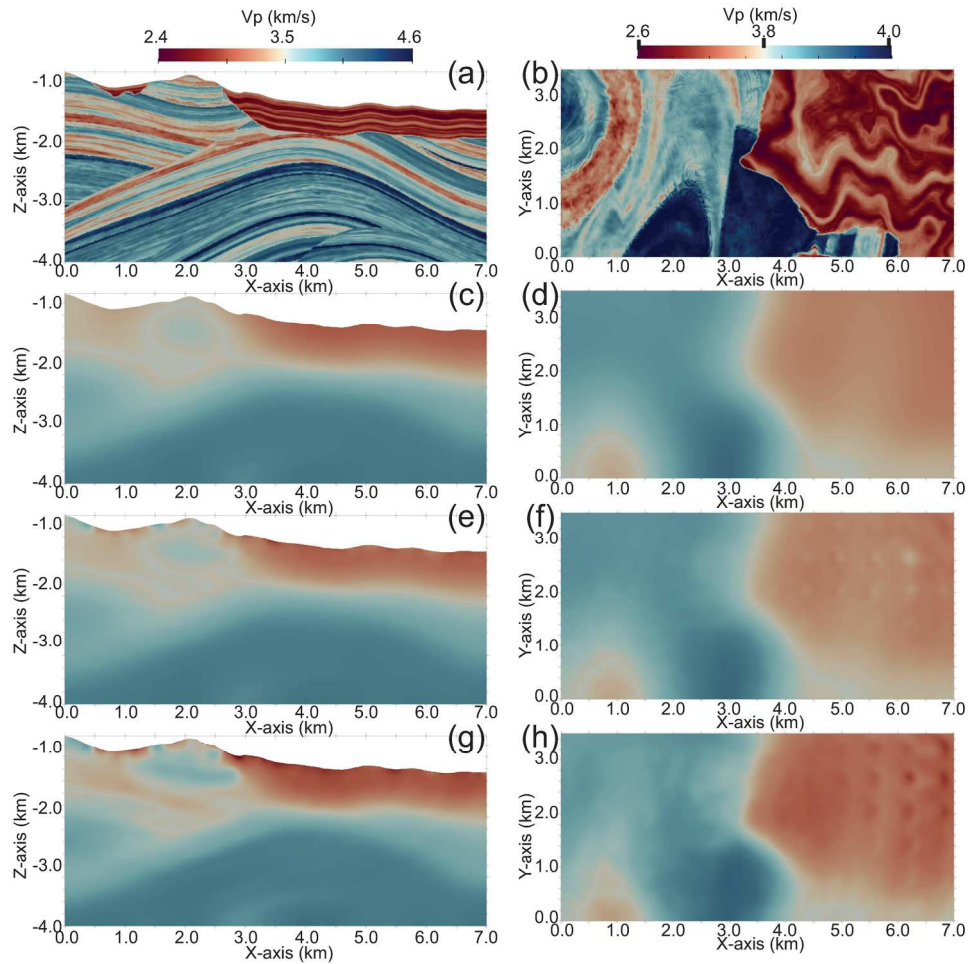
10. P wavespeed results from the first inversion example. Vertical slices at y = 1.75 km (left) and horizontal slices at 1.7 km depth (right). True (a, b), initial (c, d), envelope-difference FWI (e, f), and waveform-difference FWI (g, h) models. Note that compared to the V_S results (Figure 8), the V_P model is not as good.

195x187mm (300 x 300 DPI)
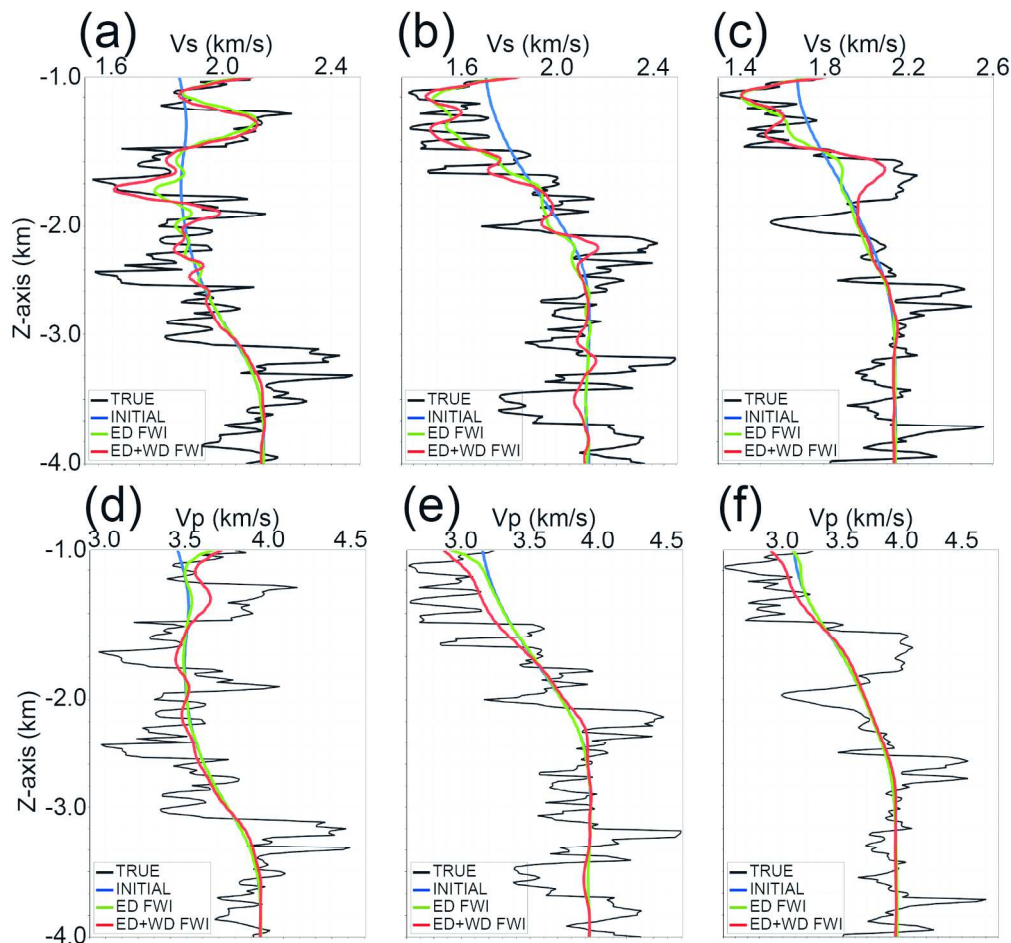
11. Vertical profiles in the target, initial, ED-FWI and final models for S (a, b and c) and P (d, e and f) wavespeeds from the first inversion example. Profiles (a) and (d) are located at x = 1.5 km and y = 1.75 km. Profiles (b) and (e) are located at x=3.5 km and y=1.75 km. Profiles (c) and (f) are located at x = 5.5 km and y = 1.75 km. Most updates are confined to the region within the first kilometre from the surface, where the V_S results are significantly improved. There are very small updates in the V_P results.

173x164mm (300 x 300 DPI)

12. Volume of investigation (VOI) function calculated for S (top) and P (bottom) wavespeeds, respectively. The computed VOI values suggest that most of reliable updates are coming from the region within 1.5 km and 0.3 km from the surface for V_S and V_P, respectively.

811x689mm (600 x 600 DPI)
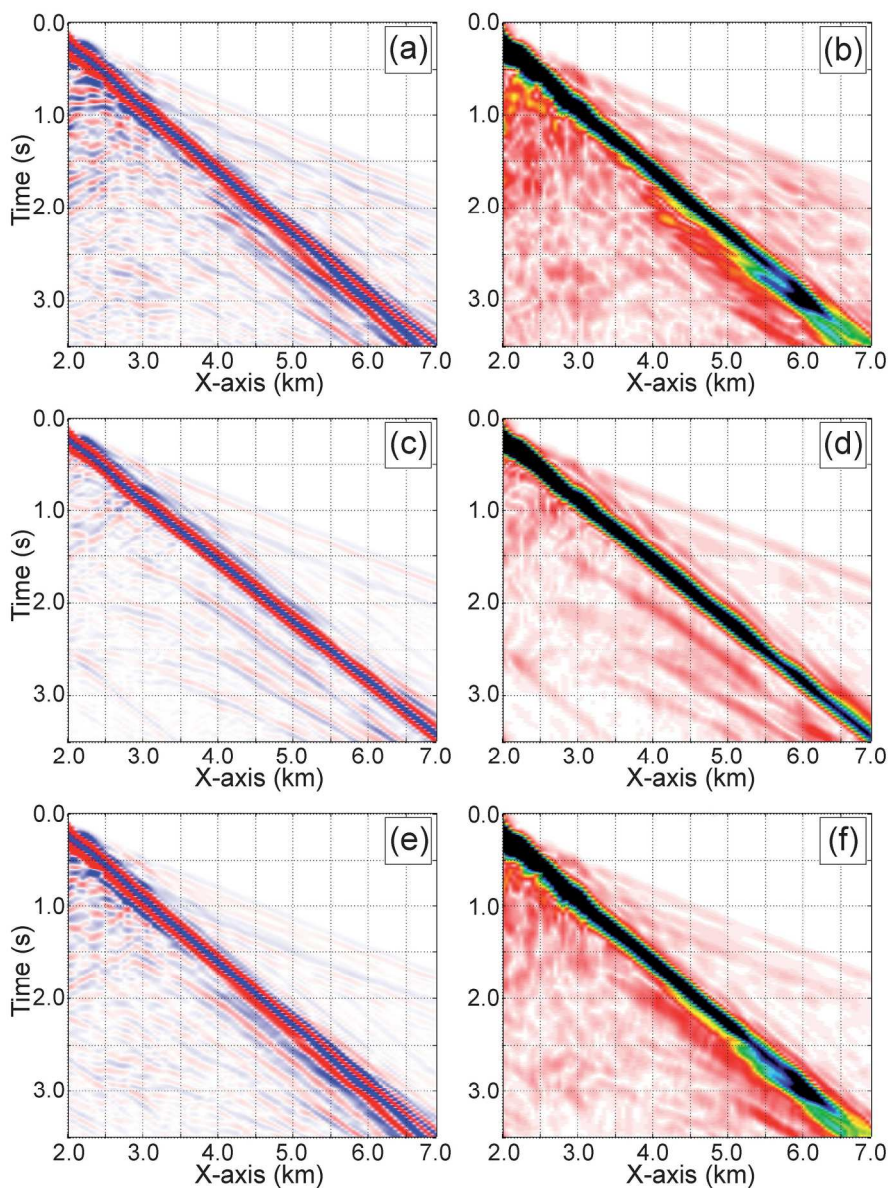
13. Trace by trace normalized shot records of vertical component of particle displacement (left) and corresponding envelopes (right) from the FWI example. Observed records (a, b), initial synthetics (c, d) and synthetics after envelope FWI (e, f). Observed data are dominated by strong amplitude and dispersive Rayleigh waves. The final synthetics agree much more closely with the observed data.

182x240mm (300 x 300 DPI)
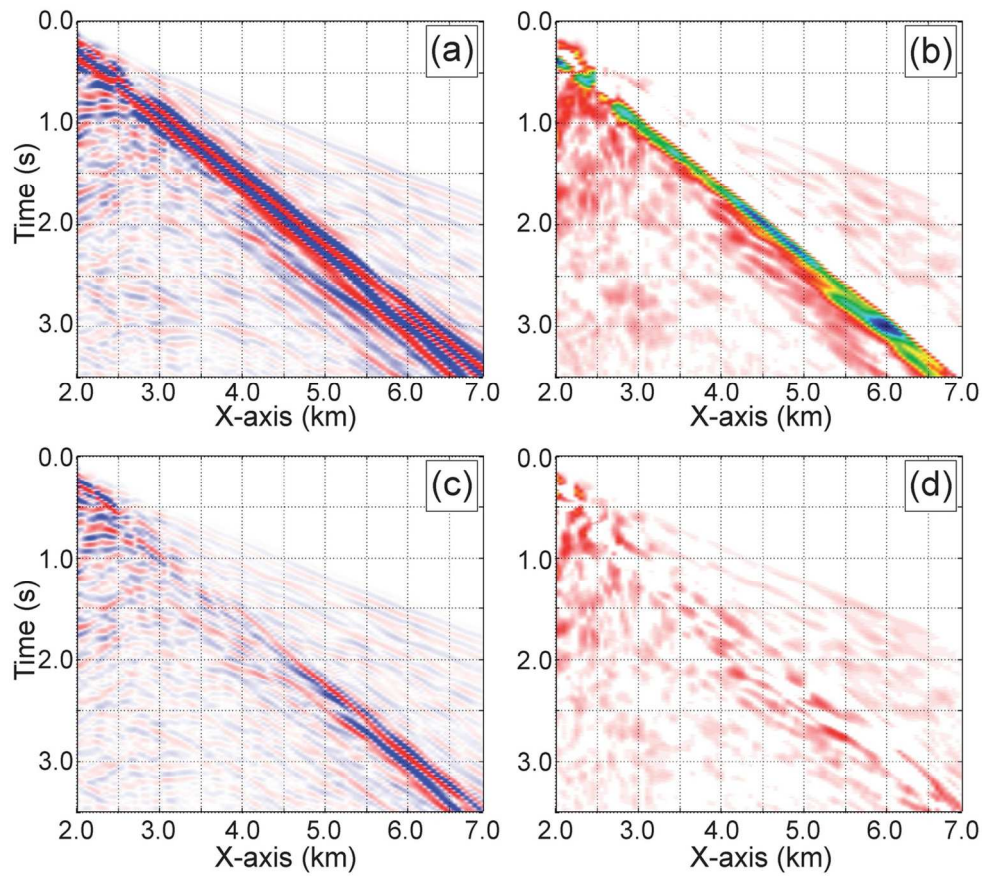
14. Initial and final data residuals (a, c); difference between observed and synthetic envelopes before (b) and after (d) inversion, respectively. In general, the amplitude of the residuals is decreased over all offsets. Additional inversion iterations might be required to further reduce residuals at near and far offsets.
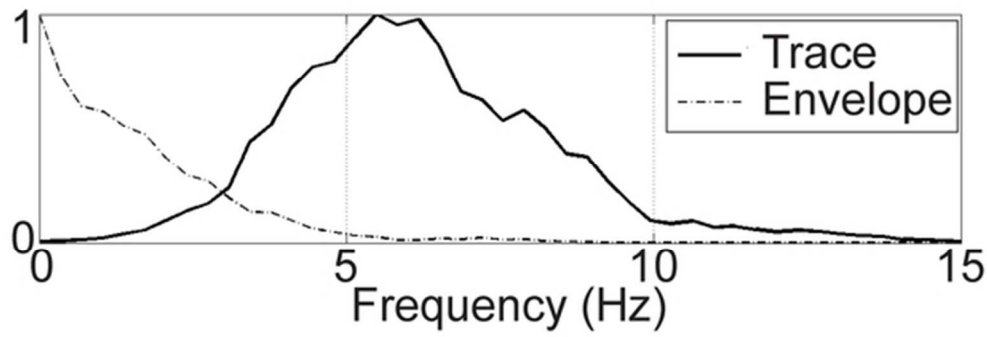
122x108mm (300 x 300 DPI)

15. Initial (left) and final (right) comparison of trace by trace normalized records of vertical component of particle displacement. Waveform (a, b) and corresponding envelope (c, d) traces. Traces are located between 2 km and 6.2 km, spaced by 0.6 km in the x-direction. At far offsets (lower part of each panel) the surface waves are cycle-skipped, whereas the difference between the corresponding envelopes is not as pronounced.
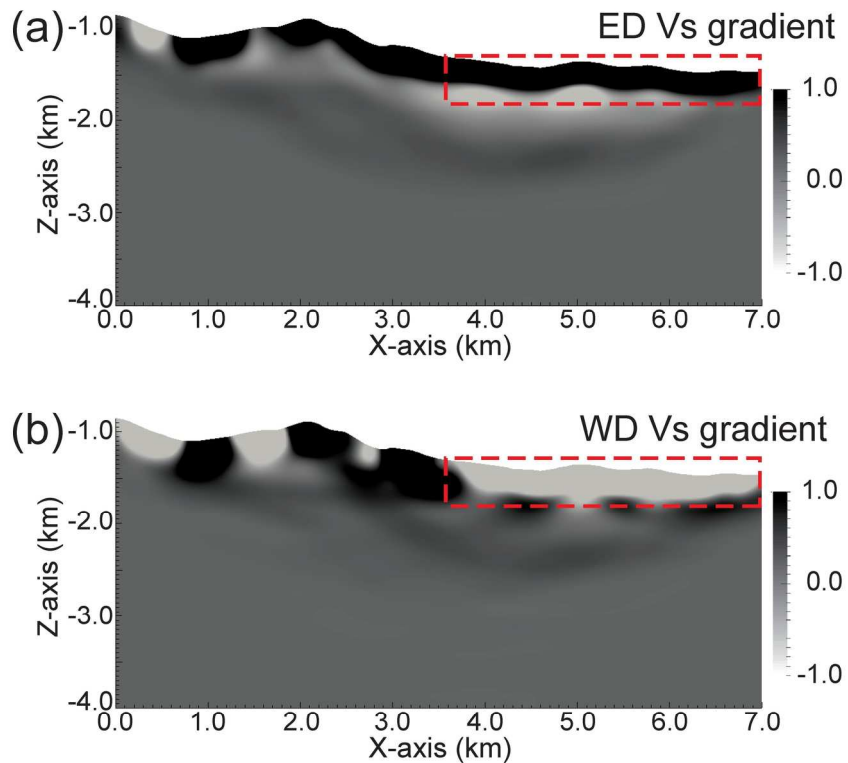
297x337mm (300 x 300 DPI)

16. Amplitude spectrum for one trace and for its envelope. The receiver is located at x = 6.0 km. Note the presence of near-zero frequencies in the envelope spectrum which promotes convergence to the global minimum.

53x18mm (300 x 300 DPI)

17. First iteration gradients of S wavespeed for envelope-difference based FWI (a) and for waveform-difference based FWI (b). The ED-FWI gradient in the shallow part on the right side (red dashed box) is positive, which enables the wavespeed reduction in that region. The WD-FWI gradient in the same area is negative, which pushes the wavespeed update in the wrong direction.
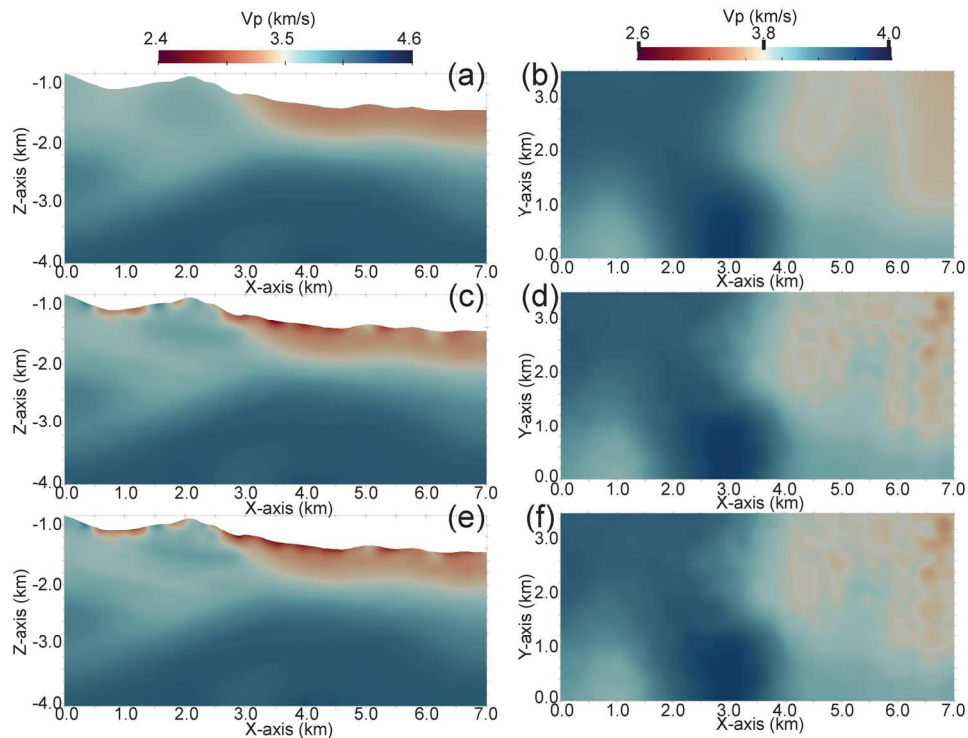
180x163mm (300 x 300 DPI)
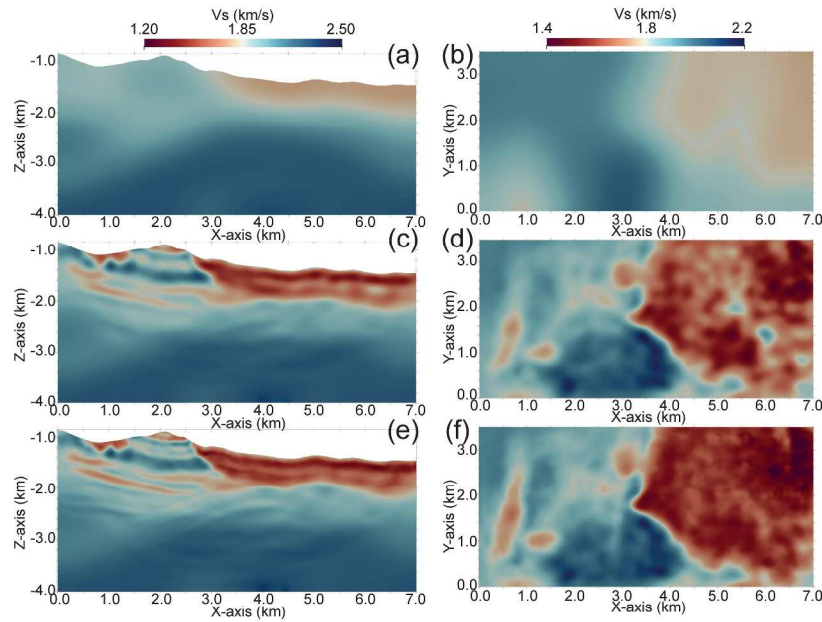
18. S wavespeed results from the second inversion experiment with a starting model increased by 5%. Vertical slices at y = 1.75 km (left) and horizontal slices at 1.7 km depth (right). Initial (a, b), envelope-difference FWI (c, d), and waveform-difference FWI (e, f) models. The overall v_S structure in the shallow part is significantly improved.

297x420mm (300 x 300 DPI)

19. P wavespeed results from the second inversion experiment with a starting model increased by 5%. Vertical slices at y = 1.75 km (left) and horizontal slices at 1.7 km depth (right). Initial (a, b), envelope-difference FWI (c, d), and waveform-difference FWI (e, f) models. Note that compared to the V_S results (Figure 18), the V_P model is not as good.

149x109mm (300 x 300 DPI)